Orbital forcing of climate 1.4 billion years ago

Shuichang Zhang[a], Xiaomei Wang[a], Emma U. Hammarlund[b], Huajian Wang[a], M. Mafalda Costa[c], Christian J. Bjerrum[d], James N. Connelly[c], Baomin Zhang[a], Lizeng Bian[e], and Donald E. Canfield[b,1]

[a]Key Laboratory of Petroleum Geochemistry, Research Institute of Petroleum Exploration and Development, China National Petroleum Corporation, Beijing 100083, China; [b]Institute of Biology and Nordic Center for Earth Evolution, University of Southern Denmark, 5230 Odense M, Denmark; [c]Centre for Star and Planet Formation, Natural History Museum of Denmark, University of Copenhagen, 1350 Copenhagen K, Denmark; [d]Department of Geosciences and Natural Resource Management, Section of Geology, and Nordic Center for Earth Evolution, University of Copenhagen, 1350 Copenhagen K, Denmark; and [e]Department of Geosciences, Nanjing University, Nanjing 210093, China

Contributed by Donald E. Canfield, February 9, 2015 (sent for review May 2, 2014)

Fluctuating climate is a hallmark of Earth. As one transcends deep into Earth time, however, both the evidence for and the causes of climate change become difficult to establish. We report geochemical and sedimentological evidence for repeated, short-term climate fluctuations from the exceptionally well-preserved ∼1.4-billion-year-old Xiamaling Formation of the North China Craton. We observe two patterns of climate fluctuations: On long time scales, over what amounts to tens of millions of years, sediments of the Xiamaling Formation record changes in geochemistry consistent with long-term changes in the location of the Xiamaling relative to the position of the Intertropical Convergence Zone. On shorter time scales, and within a precisely calibrated stratigraphic framework, cyclicity in sediment geochemical dynamics is consistent with orbital control. In particular, sediment geochemical fluctuations reflect what appear to be orbitally forced changes in wind patterns and ocean circulation as they influenced rates of organic carbon flux, trace metal accumulation, and the source of detrital particles to the sediment.

Xiamaling | Milankovitch | Mesoproterozoic | Hadley Cell | ITCZ

Many instances of climate change can be recognized through the Phanerozoic Eon (the last 542 million years). For example, fluctuating climate is well expressed in several periods of major glaciation during both the early (late Ordovician and early Silurian Periods) and late (Permian and Carboniferous Periods) Paleozoic Era (1). The causes of the early Paleozoic glaciations are not well understood, but those of the late Paleozoic Era likely resulted from a combination of low atmospheric CO_2 levels and a distribution of continents in southerly latitudes prone to the accumulation of continental ice (2). Another instance of Phanerozoic climate change includes the Paleocene–Eocene thermal maximum (3) linked to large outpourings of methane gas leading to intense global warming. Still other instances include elevated rates of volcanic CO_2 outgassing leading to global warming at the end of the Permian and Cretaceous Periods (4) and at the Triassic–Jurassic boundary (5).

During the last 2.5 million years, climate change, as recorded, for example, in glacial ice and marine sediments, was linked to periodic variations in Earth's orbit around the Sun and the controls these variations had on the amount of incoming solar radiation (insolation) reaching any point on Earth as a function of season. The orbital parameters controlling the distribution of solar insolation include the precession, or "wobble," of the Earth orbital axis, the obliquity, or tilt of the orbital axis and the eccentricity of Earth's orbit around the Sun. Precession has characteristic time scales of 19 ky (thousand years) and 23 ky, obliquity has a time scale of 41 ky, and eccentricity has a short time scale of about 100 ky and a long time scale of about 405 ky (6). The characteristic frequencies associated with these time scales are known as Milankovitch cycles (7, 8), and the advance and retreat of glacial ice through the recent Pleistocene Epoch appear to be paced to orbital forcing (9, 10).

Orbitally paced changes in solar insolation affect climate in a variety of ways, apart from the obvious expression of glaciations. For example, the intertropical convergence zone (ITCZ), the region of atmospheric upwelling near the equator, shifts its average position based on the temperature contrast between the northern and southern hemispheres, with the ITCZ migrating in the direction of the warming hemisphere (11, 12). Therefore, the ITCZ changes its position seasonally, but also on longer time scales as controlled, for example, by the latitudinal distribution of solar insolation. The position of the ITCZ correlates with the geographic distribution of wind strength and rates of precipitation, as well as patterns of ocean circulation (11, 13, 14). Changes in the position of the ITCZ are recorded, for example, in sediments of the Cariaco Basin off the coast of northern Venezuela. This site is located on the northern edge of the summer ITCZ but well north of the winter ITCZ. The geochemistry of Cariaco Basin sediments record both seasonal (15, 16) and long-term (17) changes in the position of the ITCZ—as this position influences the balance between aeolian and riverine sources of sediment to the basin, and the marine response in productivity and carbon flux to the sea floor. The longer-term variations in sediment geochemistry in the Cariaco Basin are linked to orbital forcing (17), with some variations occurring at time scales shorter than the Milankovitch cycles (15, 18).

Variations in the accumulation of organic carbon in some sediments, as these express rates of primary production, can also be attributed to these orbitally induced climate changes. For example, variations in organic carbon concentration are clearly expressed in sediments of the Cretaceous Atlantic Ocean (19–21), and these variations have been coupled to Milankovitch time scales. Indeed, broad patterns of variation in organic carbon content in sediments of the Cretaceous Atlantic Ocean seem to

Significance

There is a wealth of evidence pointing to dramatic short-term climate change on Earth over the last few million years. Much of this climate change is driven by variations of Earth's orbit around the Sun with characteristic frequencies known as Milankovitch cycles. Robust evidence for orbitally driven climate change, however, becomes rare as one descends deep into Earth time. We studied an exceptional record of climate change as recorded in 1.4-billion-year-old marine sediments from North China. This record documents regular changes in subtropical/tropical Hadley Cell dynamics. These changes in dynamics controlled wind strength, rainfall, and ocean circulation, translated into cyclic variations in sediment geochemistry, much like the orbital control on climate today and in the recent past.

Author contributions: S.Z., X.W., E.U.H., H.W., C.J.B., and D.E.C. designed research; S.Z., X.W., E.U.H., H.W., M.M.C., C.J.B., J.N.C., B.Z., L.B., and D.E.C. performed research; S.Z., X.W., E.U.H., H.W., M.M.C., C.J.B., J.N.C., and D.E.C. analyzed data; and S.Z., X.W., E.U.H., C.J.B., J.N.C., and D.E.C. wrote the paper.

The authors declare no conflict of interest.

[1]To whom correspondence should be addressed. Email: dec@biology.sdu.dk.

This article contains supporting information online at www.pnas.org/lookup/suppl/doi:10.1073/pnas.1502239112/-/DCSupplemental.

depend on paleolatitude and the location of the depositional site relative to the location of the ITCZ in the tropics and the outer, subtropical boundaries of the Hadley Cells (20, 22). Hadley Cells are one of three major cells of global atmospheric circulation resulting from the differential heating of Earth from the equator to the poles, originating as moisture-laden air rising at the ITCZ, and descending as dry air some 30° latitude north and south in the outer limbs of the Hadley Cells. The influence of Hadley Cell circulation on organic carbon accumulation is primarily related to variations in trade wind strength and rainfall intensity (20, 22). Trade wind strength controls upwelling intensity and thus rates of nutrient availability to primary producers, whereas rainfall can influence rates of nutrient delivery from the continents, thus also affecting rates of marine primary production. On orbital time scales, solar insolation shifts broad patterns of ocean and atmospheric circulation, thereby moving regions of enhanced primary production and organic carbon accumulation (23).

In pre-Phanerozoic times, conspicuous examples of climate change include the Huronian glaciations that lasted from about 2.4 billion years ago to 2.1 billion years ago (24, 25) and episodes of glaciation during the latter Neoproterozoic Eon, some of which may have been global in extent (26, 27). There are also suggestions of Milankovitch-style cyclicity in the repetitive deposition of distinct sedimentary packages linked to high-frequency sea level fluctuations (28–30). However, while the link to climate in the deposition of these sediments seems possible, the nature of the climate forcing is uncertain. Furthermore, we are unaware of any pre-Phanerozoic studies where orbital forcing has been chronologically calibrated and thus convincingly demonstrated.

We explored the ~1,400 Ma sediments of the Xiamaling Formation on the North China Craton. These rocks offer a rare glimpse into the mechanisms of climate change in the Mesoproterozoic Era (1,600 Ma to 1,000 Ma), and, with a precise chronostratigraphic framework, we are able to suggest an orbital control on climate and marine sedimentation.

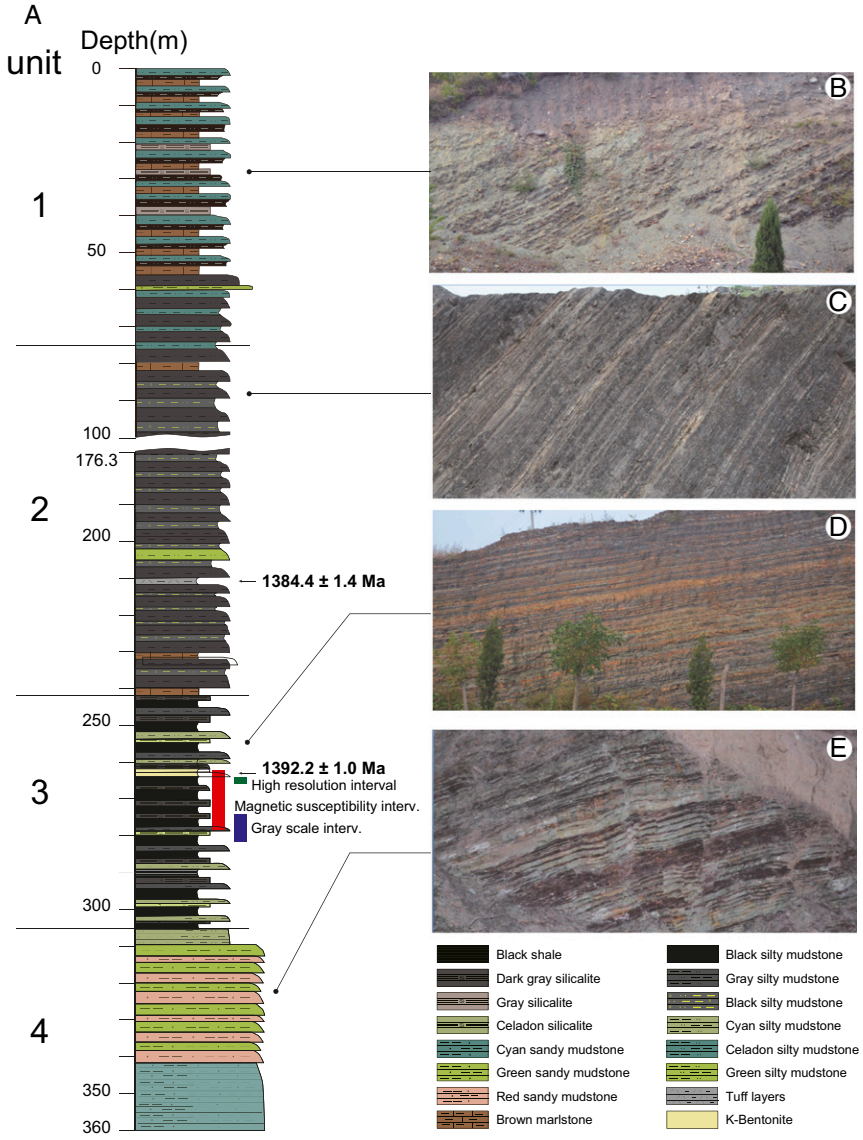

Fig. 1. Generalized stratigraphy of the Xiamaling Formation (*A*), with representative photographs of the different sedimentary units (*B–E*) demonstrating the cyclic nature of sedimentation throughout the formation. Also indicated are the locations of the section where we obtained records of magnetic susceptibility, greyscale, and high-resolution sediment geochemistry.

Depositional Setting and Sedimentology of the Xiamaling Formation

The Xiamaling Formation is part of a Paleoproterozoic (2,500–1,600 Ma) to Neoproterozoic depositional package. Sediments of the Xiamaling Formation began their deposition at ∼1,400 Ma at a paleolatitude of between 10°N and 30°N (with an uncertainty of some 10° latitude) (31, 32). There are suggestions that an active continental margin developed by the time of Xiamaling Formation deposition and that the Xiamaling Formation itself was deposited in a back-arc basin. The prime evidence for a back-arc basin setting is a series of closely spaced tuff layers at about 210 m depth in the stratigraphy (relative to a broad-scale surface unconformity; Fig. 1) and a bentonite layer 52 m below this level (33). Ash layers, however, are relatively rare in the Xiamaling Formation, and the back-arc interpretation is not certain, with little additional geological evidence to support it (34).

To provide an accurate geochronometric framework for our study, we have produced high-precision single zircon ages by isotope dilution Thermal Ionization Mass Spectrometry (TIMS) of 1,384.4 ± 1.4 Ma for the tuff and 1,392.2 ± 1.0 Ma for the bentonite layer. These ages are considerably more precise than previous SHRIMP (Sensitive High Resolution Ion Microprobe) zircon ages for the tuff of 1,367 ± 10 Ma (35, 36) and 1,377 ± 22 Ma for the bentonite layer (36, 37). Details of the dating methodology and results are summarized in *SI Text*.

The Xiamaling Formation was deposited both comformably and uncomformably onto the stromatolite-rich limestone of the Tieling Formation (33, 34), where weathering surfaces are locally preserved (34). After this, the Xiamaling Formation represents a transgressive succession having been deposited in waters deeper than storm wave base (>100 m) (33). Transgression may have resulted from downwarping associated with extensional back-arc spreading, if the back-arc basin depositional setting is correct (34). The sediment package has experienced some folding (Fig. 1), but the organic matter within the sediments is ranked as either immature or of early thermal maturity (see *SI Text*), indicating that the sediment temperatures did not likely exceed 90 °C.

The Xiamaling Formation features prominent layering of alternating sediment type through most of its thickness (Fig. 1*A*). In the lower part of the section, unit 4 comprises alternating iron oxide-rich and iron oxide-poor sediments and, in some cases, repeating bundles of alternating sediment type (Fig. 1*E*). Unit 4 has not been geochemically analyzed and will not be discussed further. The sediments of unit 4 grade upward into alternating layers of black shale and chert of unit 3 (Fig. 1*D*) and further upward into unit 2, comprised predominantly of black shale alternating with gray and black silty mudstones (Fig. 1*C*). Unit 2 sediments are tilted and not continuous in outcrop, and we estimate that 75 m of sediments are hidden from view in the subsurface. Unit 2 yields to the uppermost unit 1, composed of alternating layers of black and green shales (Fig. 1*B*). Except for the lowermost part of the Xiamaling Formation, black shales are very common, and their layering with other sediment types mostly defines the overall patterning of the rocks.

Sample Collection

All of the geochemical results reported here were obtained for samples collected along road cuts within 2–4 y after the roads were cut. The different rock types were easy to discriminate in outcrop, and all samples were collected after first removing the weathered outer layer. Except for pyrite, which was largely oxidized in the samples we collected, other aspects of sediment geochemistry were remarkably pristine, as demonstrated by comparisons with chemical analysis of fresh and unweathered core material collected at a later date in the vicinity of the outcrops (see *SI Text*). We use the core material in the present study, however, only for comparative purposes.

Outcrop samples were collected at ∼0.5-m intervals through the exposed section, with sample couplets of adjacent and contrasting rock types typically sampled. Sampling was concentrated in the upper 320 m of the stratigraphy. In addition, a high-resolution sampling profile was undertaken with approximately centimeter-scale resolution in unit 3 (depths 262.42–264.51 m; Fig. 1). We also measured magnetic susceptibility in the outcrop at Xiahuayuan village, where 292 consecutive beds were measured over 17.23 m in unit 3 (261.50–278.73 m; Fig. 1).

Biogeochemical Results

The concentrations of total organic carbon (TOC) are generally high in the black shales and reach values of nearly 20 wt% in unit 3 (Fig. 2). There is, however, spectacular variability of TOC in this unit, with concentrations fluctuating from high values of 10 wt% or more in the black shales to values of around 1 wt% or less in the adjacent layers, which are mostly cherts. High-resolution sampling from unit 3 confirms that centimeter-scale variability in rock type is accompanied by systematic variability in sediment geochemistry (Fig. 3).

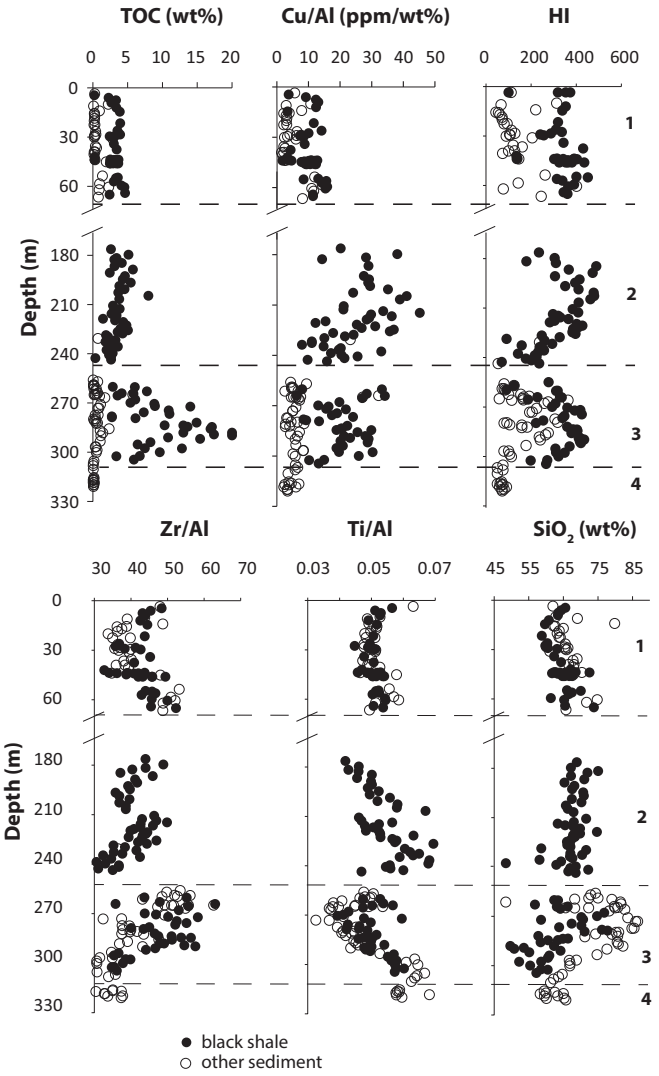

Fig. 2. Assorted geochemical parameters from the Xiamaling Formation with data from black shales indicated separately from other sediment types.

Unit 2 is composed of predominantly black shale with relatively stable TOC concentrations, whereas unit 1 exhibits TOC variability similar to that observed in unit 3, but with lower maximum TOC concentrations (Fig. 2). Variability of TOC concentrations in unit 1, as in unit 3, is correlated with sediment type, with high TOC values in the black shales and lower TOC values in the adjacent green and gray mudstones (see *SI Text* for documentation of sediment type). Hydrogen Index (HI) is a measure of organic matter quality, and patterns in HI generally follow those in TOC concentration (Fig. 2). Cu (expressed as Cu/Al) is enriched in the black shale units, and, similar to organic carbon, there is clear alternation to low Cu concentrations in the layers adjacent to the black shales in both units 1 and 3 (Fig. 2). To a small extent in unit 1 and to a large extent in unit 3, silica (Si) is enriched in the chert layers and in the mudstone layers with low TOC and trace metal levels (Fig. 2).

In unit 1, especially near the top of the unit, the Zr/Al ratio is elevated in the black shales, a feature that is even more apparent in unit 3 (Fig. 2). The Ti/Al ratio shows no real difference between rock types in unit 1, but the ratio is elevated in the black shales in unit 3 (Fig. 2). Unit 2 is predominantly black shale, and with little variability in sediment types, there is no metric to assess trends in element ratios with rock type.

A high-resolution profile from unit 3 shows centimeter-scale variability in all inorganic geochemical parameters (Fig. 3). Concentrations of Si follow lithology, with the highest concentrations in the chert layers. Ratios of Zr/Al and Ti/Al follow each other and vary inversely with Si. Ratios of Cu/Al generally vary inversely with Si, and also inversely with greytone value. Greyscale should have a strong positive relationship with TOC concentrations, and, therefore, variations in Cu/Al should also correlate with TOC, as is observed in our low-resolution profile (Fig. 2). Both K/Al and magnetic susceptibility show short-scale variability that seems to combine the patterns expressed in the other geochemical parameters. A summary of our geochemical methods and tables of our results are presented in *SI Text*.

Fluctuating Climate Recorded in the Xiamaling Formation

Except for unit 2, the Xiamaling Formation displays short-scale alternations in both rock type and chemistry (Figs. 2 and 3). Some of these chemical signals can be directly related to climate. For example, the ratios of Zr/Al, Ti/Al, and K/Al are controlled by the source of the sediment, and short time-scale variability in these ratios can reflect changes in particle sources as controlled by climate (17, 20, 21, 38, 39). Particle sources can vary both seasonally (16, 40) and over longer time scales in response to shifting patterns of rain intensity, runoff, and changes in particle wind transport (15–17, 20, 21, 38, 39).

The ratio of K/Al is sensitive to the relative mix of K-poor minerals like kaolinite and K-enriched phases like micas and clays (17, 21), while high ratios of both Ti/Al and Zr/Al are taken to reflect preferential transport of heavy minerals (for example, ilmenite, $FeTiO_3$, rutile, TiO_2 and zircon, $ZrSiO_4$) that could occur, for example, during times of arid conditions and strong winds or, alternatively, during times of high rain intensity and runoff (17, 20, 21, 38, 39, 41). We develop in the next section (*Climate Context for the Xiamaling Formation*) a climate framework for the Xiamaling Formation.

Climate Context for the Xiamaling Formation

The Xiamaling Formation shares many geochemical similarities to Cenomanian to Campanian age (~95–80 Ma) sediments from the Cretaceous Atlantic Ocean. In these sediments, distinct patterns of climate response have been related to paleolatitude and the relationship of the sites to Hadley Cell dynamics (e.g., refs. 19–21). Thus, Coniacian to Campanian age (~90–84 Ma) sediments off the present-day Ivory Coast (Ocean Drilling Program, ODP, site 959) were deposited at a paleolatitude of about 10°S (21, 22). It was argued that these sediments deposited in a high-productivity region under an ancient Hadley Cell experiencing orbitally paced alternations between wet and dry cycles (22). During wet cycles, the ITCZ was located close to the

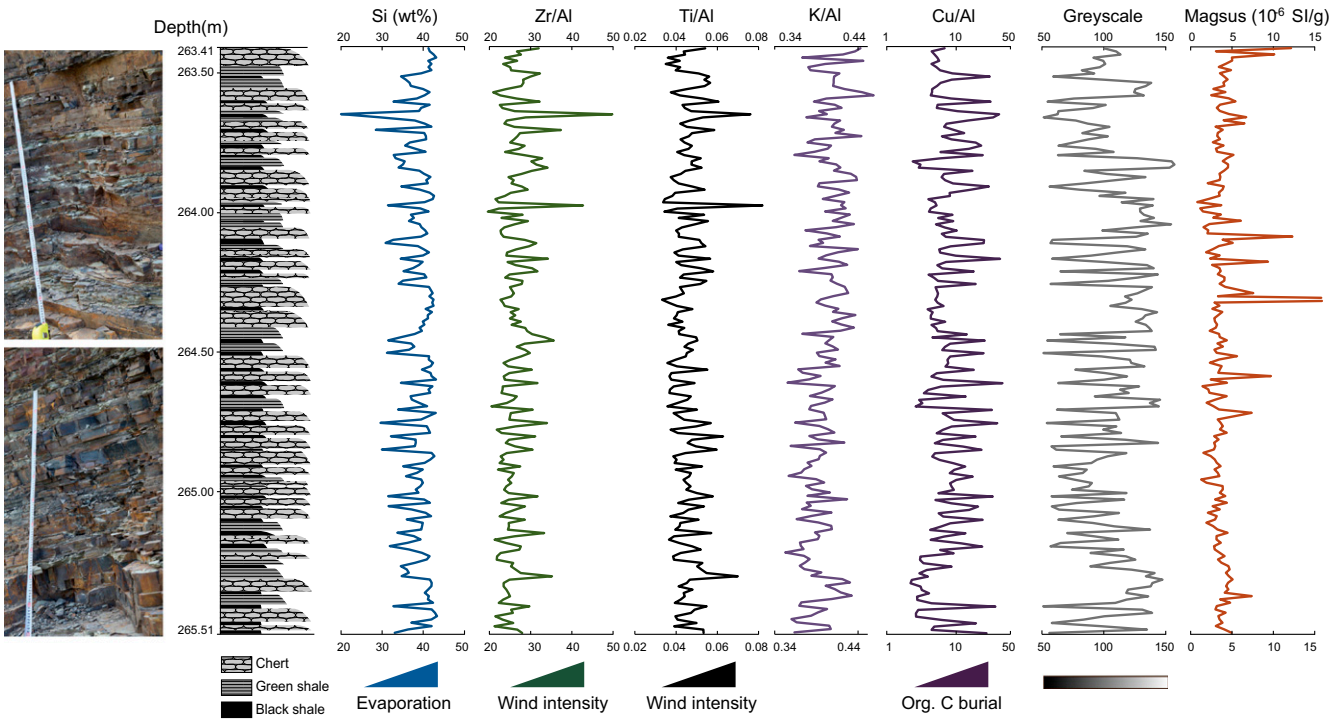

Fig. 3. High-resolution geochemistry of a 2-m section in the upper portion of unit 3 of the Xiamaling Formation. Zr/Al and Cu/Al are in units of parts per million per weight percent, while Ti/Al and K/Al are in units of weight percent/weight percent.

deposition site and high runoff from tropical Africa led to enhanced rates of marine productivity in an estuarine-type circulation, which, in turn, resulted in high concentrations of sedimentary TOC with high HI. During dry periods, northward shifts in the ITCZ resulted in reduced rates of river runoff, supporting low primary production rates and consequently low concentrations of sedimentary TOC with low HI. At this site, high wind strength during the dry cycles mobilized dense airborne particles from subtropical southern Africa, with a high Ti/Al ratio, giving a characteristic cyclic inverse relationship between TOC concentration and Ti/Al ratio (Table 1) (21, 22).

At a more northern site off tropical South America (ODP site 1261 at a paleolatitude of about 6°N), sediment deposition was argued to occur in an outer tropical location. Here, periodic shifts in the location of the ITCZ resulted in persistently high rates of primary production and organic carbon burial. High production rates were maintained through transitions between riverine-driven enhancements in primary production in the northern ITCZ, with a shift to wind-driven enhancements in production through elevated rates of upwelling as the ITCZ moved north (20, 22). At this site, HI is relatively invariant and TOC fluctuates much less than at the more southerly site, but with a positive relationship between TOC and Zr/Al (Table 1) (20). This relationship is the opposite of that recorded at the more southerly site (comparing TOC to Ti/Al in this case), suggesting that a different balance of climate dynamics was driving the patterns in sedimentation at these two sites. Indeed, it was argued that high trade winds during dry periods drove high rates of coastal upwelling and high rates of primary production at this more northerly location (20, 22). Thus, at this site, temporarily high trade wind intensity was associated with both a high depositional flux of TOC and an elevated aeolian flux of heavy particles, explaining the relationship between TOC and Zr/Al. During orbitally paced transitions to wet cycles, associated lower wind intensity reduced coastal upwelling, reducing rates of primary production and the TOC flux to the sediments. Lower wind intensity also transported less dense particles with lower Zr/Al. Continuously high HI was linked to overall enhanced TOC preservation in persistently anoxic bottom water (22, 42). Overall, the major climate control factor at this site seemed to be transitions between trade wind and river control on primary production and particle transport.

Sediments from the northerly part of the proto-North Atlantic [at a paleolatitude of about 30°N; Deep-Sea Drilling Program (DSDP) sites 105 and 603B] were argued to have been deposited in the downwelling, subtropical limb of an ancient Hadley Cell (22). In this model, orbitally driven alterations in trade wind intensity drove sedimentation dynamics. Thus, high trade wind intensity drove high rates of coastal upwelling, leading to high rates of TOC deposition as well as high HI and elevated concentrations of the redox-sensitive element Mo (19, 43). Indeed, at these northerly sites, biomarker evidence for green sulfur bacteria (44) suggests that euxinic bottom water conditions accompanied TOC, HI, and Mo-enriched black shale deposition. Interlayered green shales are TOC poor, with low HI, and they show evidence for bioturbation (19), providing strong evidence for alternations between euxinic and oxic conditions.

Overall, the strongest contrasts in geochemical properties were observed in the uprising (ODP 959) and downwelling (DSDP 105 and 603B) limbs of the Hadley Cell, with the most consistent patterns of geochemical properties in the transition zone between the two, at ODP site 1261 off Demerara Rise (22).

Depositional Model for the Xiamaling Formation

Paleomagnetic data suggest that the Xiamaling Formation was deposited in the northern tropics between about 10°N and 30°N latitude (31, 32) on the western coast of the ancient supercontinent Nuna. This position would place the Xiamaling Formation right within the influence of Hadley Cell dynamics. Beginning with unit 3, black shales contain very high concentrations of TOC, high concentrations of Cu, elevated HI, and elevated Zr/Al and Ti/Al ratios (Figs. 2 and 3 and Table 1), cycling to low values for these parameters in the adjacent cherts. These relationships are most similar to those from the proto-Atlantic influenced by fluctuating trade wind intensity as this controlled rates of upwelling, rates of primary production, and the transport of heavy minerals by wind (Table 1). The strong variations in the geochemical parameters from the Xiamaling Formation most closely resemble those from the north proto-Atlantic (DSDP sites 105 and 603B), and, by analogy, we suggest that unit 3 deposited in the downwelling, subtropical limb of an ancient Hadley Cell. Furthermore, we propose that regular changes in the position of downwelling limb of the Hadley Cell brought unit 3 under the alternating influence of high and low trade wind intensity.

The dynamics of chert precipitation are consistent with this model. In particular, chert in unit 3 was preferentially deposited in association with low TOC, low Cu, and low Zr/Al and Ti/Al rocks (Figs. 2 and 3). The Xiamaling Formation itself was deposited well before the evolution of biological Si secretion by animals (sponges) and algae (diatoms and dinoflagellates), and it is generally assumed that Proterozoic marine waters were supersaturated with Si at this time (45, 46). Therefore, marine waters would have been poised for Si oxide precipitation. Indeed, Si precipitation could have been encouraged by the net evaporation of surface seawater in dry subtropical areas under the downwelling limb of the paleo-Hadley Cell, especially during times when trade winds were reduced and marine upwelling was suppressed. The inverse relationships between Ti/Al and Si and Zr/Al and Si in the upper portion of unit 3 (Fig. 3) convincingly express the inverse relationship between times of high winds and low Si deposition and times of lower wind intensity and increased Si deposition.

Unit 2 consists of mainly black shales with stable concentrations of TOC and stable, generally high, values of HI. Fluctuations in Cu/Al, Zr/Al, and Ti/Al may exist, but they are

Table 1. Comparison of Xiamaling (XML) geochemical dynamics to sediments from the Cretaceous Atlantic

Site	Paleolatitude	TOC variability*	TOC†	Zr/Al	Ti/Al	HI
ODP 959	10°S	high	high	—	low	high
ODP 1261	6°N	Low	high	high	—	invariant
DSDP 105, 603B	30°N	high	high	—	—	high
XML unit 1	10°N–30°N	high	high	high	invariant	high
XML unit 2	10°N–30°N	low	invariant	?	?	invariant
XML unit 3	10°N–30°N	high	high	high	high	high

Dashes mean no data, and question marks mean the behavior is impossible to characterize, as TOC is invariant.
*An indication of whether TOC variability is high or low in the section.
†For the columns to the right (Zr/Al, Ti/Al, HI), the behavior is given when TOC is high (as indicated in this column), except for XML unit 2, where the TOC is relatively invariant.

difficult to identify through the monotonous deposition of black shale and with our rather coarse interval sampling of this unit. Despite this limitation, the depositional dynamics are different and less variable than in unit 3, and, by analogy with the model developed for the Cretaceous Atlantic, this part of the Xiamaling Formation may have been deposited in a transitional outer tropical zone with influence from both wind-driven upwelling and ITCZ-driven runoff. Indeed, unit 2 shares many similarities in geochemical behavior to ODP site 1261 (Table 1).

Unit 1 shares some similarities with unit 3. Periodic alterations with sediment type in TOC, HI, Zr/Al, Cu/Al, and SiO_2 resemble those in unit 3, but the magnitudes of the changes are generally more modest in unit 1 than in unit 3. In addition, unlike unit 3, there is no variation in Ti/Al with sediment type. Still, a positive relationship between high TOC and elevated Zr/Al would be consistent with elevated winds during the time of high TOC deposition. Overall, while the geochemical signals are not as strong in unit 1 as in unit 3, they are consistent with sediment deposition under the downwelling limb of a paleo-Hadley Cell. Therefore, as for unit 3, we propose that periodic fluctuations in trade wind intensity regulated rates of upwelling, rates of primary production, and the chemistry of particles transported to the basin.

The geochemical and sedimentological records from the Xiamaling Formation seem to express deposition under different portions of an ancient Hadley Cell promoted by long-term (millions of years) shifts in the position of the ITCZ. In this view, the transition between unit 3 and unit 2 represents a northward migration of the ITCZ and a subsequent northern migration of the position of the ancient Hadley Cell. This migration would have moved the depositional site of the Xiamaling Formation from the core downwelling part of the northern Hadley Cell with dominant influence of the ITCZ to the transitional part in the outer tropics, where both ITCZ runoff and wind-driven upwelling alternated. Unit 1, then, could represent migration back to a more southerly, full tropical location, bringing the Xiamaling Formation once again under the direct influence of the ITCZ. Tectonic drift of the North China Block during Xiamaling deposition could have also contributed, in part, to changes in the location of deposition relative to location of the ancient Hadley Cell.

Orbital Forcing of Deposition

Numerous numerical models have shown that meridional patterns of precipitation rate, trade wind strength, and rates of ocean upwelling are sensitive to both the intensity and latitudinal distribution of solar insolation (13, 14, 21, 47–49). We extend this analogy to the Xiamaling Formation, and hypothesize that orbitally induced forcing of climate was also active in the Mesoproterozoic Era, thus providing a mechanism for the observed repetitive patterns of sedimentation.

We test for periodicity in unit 3 sedimentation by analyzing relatively long records of greyscale data from an outcrop photograph (see *SI Text*), a lower-resolution magnetic susceptibility record (see *SI Text*), as well the relatively short, but high-resolution, geochemical records in Fig. 3. It has been shown that greyscale data are well suited for spectral analysis, as tone differences reflect variability in sediment type and/or geochemistry (for example, dark TOC-rich layers and light Si-dominated layers; Fig. 3) (50). Magnetic susceptibility reflects changes in magnetic mineral content that could relate to both changes in the input of detrital magnetic minerals (magnetite, for example) and changes in the geochemical environment as it controls, through diagenesis, both the formation and dissolution of magnetic minerals (51, 52). Details of how we generated our long records of magnetic susceptibility and greyscale are found in *SI Text*.

All of our data were analyzed in Matlab using the multitaper method (MTM) to generate periodograms for estimating power spectra (53). Before analysis, the magnetic susceptibility record was linearly interpolated to a uniform sample spacing of 0.5 cm, similar to the greyscale image. Then, both the magnetic susceptibility and greyscale data were band-pass filtered with a Butterworth filter of order 5 using half power frequencies of 1/5 m^{-1} and 1/0.01 m^{-1}, removing periods longer than ~8 m and shorter than ~1 cm. This procedure removed long-term trends, and small-scale noise from displaced sediments and rock fractures on the outcrop photo. The high-resolution geochemical record was low-pass filtered with a Butterworth filter of order 5 using a half-power frequency of 1/5 m^{-1}. The MTM periodograms of a selection of the band-pass-filtered data are presented in Fig. 4, whereas the other periodograms are presented in *SI Text*.

Random, nonperiodic variations in the climate system, such as some of the dynamics associated with ocean circulation or sedimentary depositional processes, are quite common in nature, resulting in apparent periodicities giving rise to a red noise power spectrum (54). This generates a problem of discriminating true periodicities from red noise variation. Here, we use two types of noise models to estimate the significance of the periodogram peaks.

Following the methods outlined in refs. 55–57, we estimated the significance of peaks relative to the commonly used robust red noise model generated by a univariate lag-1 autoregressive process where the two constants of the mean red noise model were fit by least-squares error to the median smoothed periodogram (54, 57).

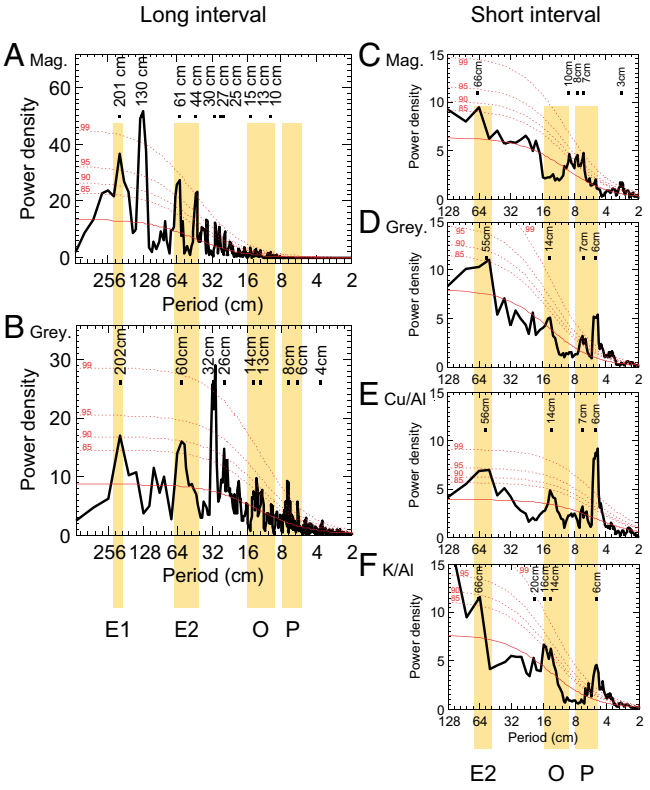

Fig. 4. Spectral analysis by MTM of (*A*) magnetic susceptibility of unit 3 of the Xiamaling Formation in the depth interval of 261.50–278.73 m and (*B*) greyscale trace of outcrop photograph in the depth interval of 278–285 m. MTM periodogram (black line) of the band-pass-filtered series computed using two tapers. Median fitted first-order autoregressive noise model (red line) and 85%, 90%, 95%, and 99% confidence level estimates (red dashed lines) following refs. 55–57. Interpreted Milankovitch orbital periodicities are long and short eccentricity (E1, E2), obliquity (O) and precession (P) based on average formation sedimentation rates derived from dated volcanic beds. Note that magnetic susceptibility reflects geochemical changes such as variations in magnetic minerals gregite–magnetite expected to vary relative to ferrouginous–euxinic condition. (*C*–*F*) Spectral analyses of the short high-resolution geochemical records are presented: (*C*) magnetic susceptibility, (*D*) greyscale, (*E*) Cu/Al, and (*F*) K/Al.

We calculated the 85–99% confidence level (from procedure in ref. 55) to assess whether the periodogram peaks are statistically different from the mean red noise model. We also tested our band-pass-filtered data toward a noise model with a bending power-law spectrum noise model (see *SI Text* for further details). As before, the constants of the noise model were fit by least-squares error to the median smoothed periodogram (54). We find that the robust red noise model has a smaller least-squares error toward the median smoothed periodogram than the bending power-law spectrum noise model.

The MTM periodograms have several significant peaks exceeding the 90% confidence level relative to the mean robust red noise spectrum as well as the power-law noise model (Fig. 4, see *SI Text*, and Table 2). Ideally, the 99% confidence level ensures the lowest chance for a false positive identification of periodicities. We use, however, several independent data sets, and as we detect very similar periodicities in these, we suggest that a lower confidence level may be used to identify true periodicity in our various data records.

Both the long magnetic susceptibility and greyscale records display periodicities in the range of 201–202 cm, 60–62 cm, 26–32 cm, and 12–16 cm, while the long greyscale and all of the short records reveal periodicity in the range of 6–8 cm. Some of the short records, like the long records, display periodicity in the range of 42–66 cm and 10–14 cm with additional periodicity at 3 cm (Fig. 4, *SI Text*, and Table 2).

Our new geochronometry allows us to convert these periodicities into approximate time scales. Thus, the 52 m separating the bentonite and tuff layers deposited over a time interval of 7.9 ± 1.7 Ma (uncertainty from combining the errors in quadrature), yield an average sedimentation rate of 0.66 ± 0.14 cm·ky^{-1}. Assuming this sedimentation applies, in general, for the upper part of unit 3, the ~202-cm period corresponds to 305 ± 65 ky, periods in the range of 42–62 cm correspond to 63–94 ± 20 ky, and the 10- to 16-cm periods correspond to 15–24 ± 5 ky and the 6- to 8-cm periods correspond to 9–12 ± 2 ky. Earth's long orbital eccentricity of 405 ky is considered unchanged over geological time, representing the metronome of astronomical forcing (58). Accepting this, our longest period from the Xiamaling Formation, at 305 ± 65 ky, is close to the orbital long eccentricity cycle. In our view, this similarity in period length is not a coincidence. Indeed, if the sections analyzed for greyscale and magnetic susceptibility maintained just a 10% lower sedimentation rate than the 0.66 ± 0.14 cm·ky^{-1} average for the 52-m section immediately above (see Fig. 1), then our longest periodicity would overlap the 405-ky-long eccentricity cycle. We believe that this is likely and that the sediments of the Xiamaling Formation record eccentricity forcing from Earth's orbit around the Sun.

If we accept that the 202-cm period records the 405-ky-long eccentricity cycle, then the periods from 42 to 62 cm reflect a time scale of 84–124 ky, the 10- to 16-cm period corresponds to 20–32 ky, and the 6- to 8-cm period corresponds to 12–16 ky. The shorter two of these periods correspond well to the obliquity (21–30 ky) and precession (14–17 ky) time scales as expected at 1,400 Ma by recalculation from ref. 59 (see *SI Text*). The 84- to 124-ky period overlaps the present short eccentricity period of 95–131 ky (6).

In addition to these periods, there is also strong periodicity at 130 cm in the long magnetic susceptibility record, corresponding to 260 ky, with additional periodicities of 25–32 cm, and 3 cm in some of the periodograms (Fig. 4, *SI Text*, and Table 2). These additional periods correspond to time scales of 50–64 ky and 6 ky. Of these, the 50- to 64-ky periods are half of the short eccentricity period, and the 6-ky period is a half precession period. While the 260-ky period is enigmatic, the periods representing one half of the eccentricity and precession cyles could arise as the ITCZ passed twice over the site of deposition in moving from one position to a new position and back again.

Taken together, the periodicity of Xiamaling Formation sedimentation appears to record all of the major periods expected from the orbital forcing of solar insolation on Earth. Thus, like today and like much of the Phanerozoic Eon, orbital forcing exhibited a strong influence on tropical–subtropical climate 1.4 billion years ago.

Table 2. Summary of periodicities (in centimeters) for data from the short (2.1 m) and long (17.3-m magnetic susceptibility and 7.2-m greyscale) records

Magnetic susceptibility		Greyscale		Cu/Al	Si	Zr/Al	Ti/Al	K/Al	Suggested orbital time scale, ky[¶]	Suggested orbital periodicity
17.3-m interval	2.1-m interval	7.2-m interval	2.1-m interval	2.1-m interval	2.1-m interval	2.1-m interval	2.1-m interval	2.1-m interval		
201*		202[†]							405	E1
130									261	
61*	66[‡]	60[†]					66[†]	66[†]	128	
			55[‡]	56*	58[§]				113	E2
44						42[†]			86	
30		32							62	
27									54	E2/2
25		26[†]			26[†]				52	
15		14						16[†]	30	
13		13[†]	14[§]	14[‡]	14[‡]			14*	27	O
10	10[†]				11[§]		11[‡]		21	
	8	8							16	
	7		7*	7[§]	7[†]	7[§]	7[†]	7	14	P
		6	6	6	6	6	6	6	12	
	3	4	3					4	7	P/2

Alternating shading groups time scales of the same suggested periodicity. Unless noted, confidence limit is 99%. E1, long eccentricity; E2, short eccentricity, E2/2, half short eccentricity; O, obliquity; P, precession; P/2, half precession.
*Confidence limit is 95%.
[†]Confidence limit is 90%.
[‡]Confidence limit is 85%.
[§]Periodicity above red noise and similar to periodicities noted as significant (>85%) in other peridigrams.
[¶]Periodicities (centimeters as averaged along horizontal line) converted to time scales (kiloyears) assuming that the 202-cm period corresponds to the long eccentricity (E1) of 405 ky.

Conclusions

The Xiamaling Formation affords a rare look into pre-Phanerozoic climate, and particularly during the Mesoproterozoic Era where virtually nothing of Earth's climate is known. We observe climate fluctuations that resemble those recorded in sediments from the Cretaceous Atlantic and the recent Cariaco Basin. On long time scales, climate change produced differences in sediment geochemistry consistent with periodic migration of the ITCZ, as this controlled Hadley Cell dynamics and the intensities of rainfall, trade wind intensity, and rates of marine upwelling at the site of Xiamaling Formation deposition. Using a well-constrained chronological framework, we demonstrated that periodic changes in sediment chemistry were likely controlled by the orbital forcing of climate on Milankovitch time scales.

ACKNOWLEDGMENTS. We thank Huitong Wang, Dina Holmgaard Skov, Heidi Grøn Jensen, and Susanne Møller for technical support, as well as Gordon R. J. Cooper for advice and scripts on signal processing. Linda Hinnov is acknowledged for comments on an earlier draft, and both Adam Maloof and Thomas Wagner are thanked for valuable comments and suggestions. We thank the Danish National Research Foundation (Grant DNRF53), the European Research Council (Oxygen Grant 267233), the Danish Agency for Science, Technology and Innovation (Grant 12-125692), the PetroChina Science and Technology Projects (Grants 2011A-0201 and 2014A-2011), and the National 973 Basic Research Program of China (G1999043306).

1. Frakes LA, Francis JE (1988) A guide to Phanerozoic cold polar climates from high-latitude ice-rafting in teh Cretaceous. *Nature* 333:547–549.
2. Bender ML (2013) *Paleoclimate* (Princeton Univ Press, Princeton).
3. Dickens GR (2011) Down the Rabbit Hole: Toward appropriate discussion of methane release from gas hydrate systems during the Paleocene-Eocene thermal maximum and other past hyperthermal events. *Clim. Past.* 7(3):831–846.
4. Wignall PB (2001) Large igneous provinces and mass extinctions. *Earth Sci Rev* 53(1-2):1–33.
5. Beerling DJ, Berner RA (2002) Biogeochemical constraints on the Triassic-Jurassic boundary carbon cycle event. *Global Biogeochem Cycles* 16(3), 10.1029/2001GB001637.
6. Hinnov LA, Hilgen FJ (2012) Cyclostratigraphy and astrochronology. *The Geologic Time Scale 2012*, eds Gradstein FM, Ogg JG, Schmitz M, Ogg GM (Elsevier, Amsterdam), Vol 1, pp 63–83.
7. Milankovitch M (1920) *Théorie Mathématique des Phénomènes Thermiques Produits par la Radiation Solaire* (Gauthier-Villars, Paris).
8. Berger A, Loutre MF, Tricot C (1993) Insolation and Earth's orbital periods. *J Geophys Res* 98(D6):10341–10362.
9. Milankovitch M (1941) *Kanon der Erdbesrtrahlung und seine Anwendung auf das Eiszeitenproblem* (Mihaila Ćurčića, Belgrade).
10. Hays JD, Imbrie J, Shackleton NJ (1976) Variations in Earth's orbit: Pacemaker of the ice ages. *Science* 194(4270):1121–1132.
11. Broccoli AJ, Dahl KA, Stouffer RJ (2006) Response of the ITCZ to Northern Hemisphere cooling. *Geophys Res Lett* 33(1):LO1702.
12. Schneider T, Bischoff T, Haug GH (2014) Migrations and dynamics of the intertropical convergence zone. *Nature* 513(7516):45–53.
13. Sloan LC, Huber M (2001) Eocene oceanic responses to orbital forcing on precessional time scales. *Paleoceanography* 16(1):101–111.
14. Clement AC, Hall A, Broccoli AJ (2004) The importance of precessional signals in the tropical climate. *Clim Dyn* 22(4):327–341.
15. Haug GH, Hughen KA, Sigman DM, Peterson LC, Röhl U (2001) Southward migration of the intertropical convergence zone through the Holocene. *Science* 293(5533):1304–1308.
16. Martinez NC, et al. (2007) Modern climate forcing of terrigenous deposition in the tropics (Cariaco Basin, Venezuela). *Earth Planet Sci Lett* 264(3-4):438–451.
17. Yarincik KM, Murray RW, Peterson LC (2000) Climatically sensitive eolian and hemipelagic deposition in the Cariaco Basin, Venezuela, over the past 578,000 years: Results from Al/Ti and K/Al. *Paleoceanography* 15(2):210–228.
18. Gibson KA, Peterson LC (2014) A 0.6 million year record of millennial-scale climate variability in the tropics. *Geophys Res Lett* 41(3):969–975.
19. Kuypers MMM, et al. (2004) Orbital forcing of organic carbon burial in the proto-North Atlantic during oceanic anoxic event 2. *Earth Planet Sci Lett* 228(3-4):465–482.
20. Hofmann P, Wagner T (2011) ITCZ controls on Late Cretaceous black shale sedimentation in the tropical Atlantic Ocean. *Paleoceanography* 26(4):PA4223.
21. Beckmann B, Flögel S, Hofmann P, Schulz M, Wagner T (2005) Orbital forcing of Cretaceous river discharge in tropical Africa and ocean response. *Nature* 437(7056):241–244.
22. Wagner T, Hofmann P, Flogel S (2013) Marine black shale deposition and Hadley Cell dynamics: A conceptual framework for the Cretaceous Atlantic Ocean. *Mar Pet Geol* 43:222–238.
23. Meyers SR, Sageman BB, Arthur MA (2012) Obliquity forcing of organic matter accumulation during Oceanic Anoxic Event 2. *Paleoceanography* 27(3):PA3212.
24. Eyles N (1993) Earth's glacial record and its tectonic setting. *Earth Sci Rev* 35(1-2): 1–248.
25. Bekker A, Kaufman AJ (2007) Oxidative forcing of global climate change: A biogeochemical record across the oldest Paleoproterozoic ice age in North America. *Earth Planet Sci Lett* 258:486–499.
26. Kirschvink JL (1992) Late Proterozoic low-latitude global glaciation: The snowball Earth. *The Proterozoic Biosphere*, eds Schopf JW, Klein C (Cambridge Univ Press, Cambridge, UK), pp 51–58.
27. Hoffman PF, Kaufman AJ, Halverson GP, Schrag DP (1998) A neoproterozoic snowball Earth. *Science* 281(5381):1342–1346.
28. Grotzinger JP (1986) Upward shallowing platform cycles: A response to 2.2 billion years of low-amplitude, high-frequency (Milankovitch band) sea level oscillations. *Paleoceanography* 1(4):403–416.
29. Mei MX, Ma YS, Guo QY (2001) Basic lithofacies-succession model for the Wumishan cyclothems: Their Markov chain analysis and regularly vertical stacking patterns in the third-order sequences. *Acta Geol Sin (Engl Ed)* 75(4):421–431.
30. Hofmann A, Dirks P, Jelsma HA (2004) Shallowing-upward carbonate cycles in the Belingwe Greenstone Belt, Zimbabwe: A record of Archean sea-level oscillations. *J Sediment Res* 74(1):64–81.
31. Zhang SH, et al. (2012) Pre-Rodinia supercontinent Nuna shaping up: A global synthesis with new paleomagnetic results from North China. *Earth Planet Sci Lett* 353:145–155.
32. Evans DAD, Mitchell RN (2011) Assembly and breakup of the core of Paleoproterozoic-Mesoproterozoic supercontinent Nuna. *Geology* 39(5):443–446.
33. Meng QR, Wei HH, Qu YQ, Ma SX (2011) Stratigraphic and sedimentary records of the rift to drift evolution of the northern North China craton at the Paleo- to Mesoproterozoic transition. *Gondwana Res* 20(1):205–218.
34. Qu Y, et al. (2014) Geological characteristics and tectonic significance of unconformities in Mesoproterozoic successions in the northern margin of the Northern China Block. *Geosci Front* 5:127–138.
35. Gao LZ, et al. (2008) Mesoproterozoic age for Xiamaling Formation in North China Plate indicated by zircon SHRIMP dating. *Chin Sci Bull* 53(17):2665–2671.
36. Li HK, et al. (2013) Recent advances in the study of the Mesoproterozoic geochronology in the North China Craton. *J Asian Earth Sci* 72:216–227.
37. Su WB, et al. (2008) SHRIMP U-Pb ages of K-bentonite beds in the Xiamaling Formation: Implications for revised subdivision of the Meso- to Neoproterozoic history of the North China Craton. *Gondwana Res* 14(3):543–553.
38. Shimmield GB, Mowbray SR, Weedon GP (1990) A 350 ka history of the Indian Southwest Monsoon—Evidence from deep-sea cores, Northwest Arabian Sea. *Trans R Soc Edinburgh Earth Sci* 81(4):289–299.
39. Boyle EA (1983) Chemical accumulation variations under the Peru Current during the past 130,000 years. *J Geophys Res* 88(C12):7667–7680.
40. Shao JQ, Yang SY (2012) Does chemical index of alteration (CIA) reflect silicate weathering and monsoonal climate in the Changjiang River basin? *Chin Sci Bull* 57(10):1178–1187.
41. Rea DK, Snoeckx H, Joseph LH (1998) Late Cenozoic eolian deposition in the North Pacific: Asian drying, Tibetan uplift, and cooling of the Northern Hemisphere. *Paleoceanography* 13(3):215–224.
42. März C, et al. (2008) Redox sensitivity of P cycling during marine black shale formation: Dynamics of sulfide and anoxic, non-sulfidic bottom waters. *Geochim Cosmochim Acta* 72:3703–3717.
43. Tribovillard N (2006) Trace metals as paleoredox and paleoproductivity proxies: An update. *Chem Geol* 232(1-2):12–32.
44. Kuypers MMM, Pancost RD, Nijenhuis IA, Damste JSS (2002) Enhanced productivity led to increased organic carbon burial in the euxinic North Atlantic basin during the late Cenomanian oceanic anoxic event. *Paleoceanography* 17(4):1051.
45. Konhauser KO, Lalonde SV, Amskold L, Holland HD (2007) Was there really an Archean phosphate crisis? *Science* 315(5816):1234.
46. Siever R (1992) The silica cycle in the Precambrian. *Geochim Cosmochim Acta* 56(8): 3265–3272.
47. Winguth A, Winguth C (2013) Precession-driven monsoon variability at the Permian-Triassic boundary—Implications for anoxia and the mass extinction. *Global Planet Change* 105:160–170.
48. Yoshimori M, Broccoli AJ (2008) Equilibrium response of an atmosphere-mixed layer ocean model to different radiative forcing agents: Global and zonal mean response. *J Clim* 21(17):4399–4423.
49. Yoshimori M, Broccoli AJ (2009) On the link between Hadley circulation changes and radiative feedback processes. *Geophys Res Lett* 36(20):L20703.
50. Hinnov LA (2013) Cyclostratigraphy and its revolutionizing applications in the Earth and planetary sciences. *Geol Soc Am Bull* 125:1703–1734.
51. Canfield DE, Berner RA (1987) Dissolution and pyritization of magnetite in anoxic marine sediments. *Geochim Cosmochim Acta* 51:645–659.
52. Karlin R, Lyle M, Heath GR (1987) Authigenic magnetite formation in suboxic marine sediments. *Nature* 326(6112):490–493.
53. Thomson DJ (1982) Spectrum estimation and harmonic analysis. *Proc IEEE* 70(9):1055–1096.
54. Vaughan S, Bailey RJ, Smith DG (2011) Detecting cycles in stratigraphic data: Spectral analysis in the presence of red noise. *Paleoceanography* 26(4):PA4211.
55. Torrence C, Compo GP (1998) A practical guide to wavelet analysis. *Bull Meteorol Soc* 79(1):61–78.
56. Mann ME, Lees JM (1996) Robust estimation of background noise and signal detection in climatic time series. *Clim Change* 33(3):409–445.
57. Meyers SR (2012) Seeing red in cyclic stratigraphy: Spectral noise estimation for astrochronology. *Paleoceanography* 27(3):PA3228.
58. Berger A, Loutre MF, Laskar J (1992) Stability of the astronomical frequencies over Earth's history for paleoclimatic studies. *Science* 255(5044):560–566.
59. Walker JCG, Zahnle KJ (1986) Lunar nodal tide and distance to the Moon during the Precambrian. *Nature* 320(6063):600–602.